



# Perfect absorption in GaAs metasurfaces near the bandgap edge

L. L. HALE,<sup>1,\*</sup>  P. P. VABISCHEVICH,<sup>2,4,5</sup>  T. SIDAY,<sup>1,6</sup> C. T. HARRIS,<sup>2,3</sup> T. S. LUK,<sup>2,3</sup> S. J. ADDAMANE,<sup>2,3</sup> J. L. RENO,<sup>2,3</sup> I. BRENER,<sup>2,3</sup> AND O. MITROFANOV<sup>1,2</sup>

<sup>1</sup>University College London, Electronic and Electrical Engineering, London WC1E 7JE, United Kingdom

<sup>2</sup>Center for Integrated Nanotechnologies, Sandia National Laboratories, Albuquerque, New Mexico 87123, USA

<sup>3</sup>Sandia National Laboratory, Albuquerque, New Mexico 87185, USA

<sup>4</sup>Present affiliation: Physical Measurement Laboratory, National Institute of Standards and Technology, Gaithersburg, MD 20899, USA

<sup>5</sup>Present affiliation: Institute for Research in Electronics and Applied Physics & Maryland NanoCenter, University of Maryland, College Park, MD 20742, USA

<sup>6</sup>Present affiliation: Institut für Experimentelle und Angewandte Physik, Universität Regensburg Universitätsstraße, Regensburg 31 93053, Germany

\*[lucy.hale@ucl.ac.uk](mailto:lucy.hale@ucl.ac.uk)

**Abstract:** Perfect optical absorption occurs in a metasurface that supports two degenerate and critically-coupled modes of opposite symmetry. The challenge in designing a perfectly absorbing metasurface for a desired wavelength and material stems from the fact that satisfying these conditions requires multi-dimensional optimization often with parameters affecting optical resonances in non-trivial ways. This problem comes to the fore in semiconductor metasurfaces operating near the bandgap wavelength, where intrinsic material absorption varies significantly. Here we devise and demonstrate a systematic process by which one can achieve perfect absorption in GaAs metasurfaces for a desired wavelength at different levels of intrinsic material absorption, eliminating the need for trial and error in the design process. Using this method, we show that perfect absorption can be achieved not only at wavelengths where GaAs exhibits high absorption, but also at wavelengths near the bandgap edge. In this region, absorption is enhanced by over one order of magnitude compared a layer of unstructured GaAs of the same thickness.

Published by The Optical Society under the terms of the [Creative Commons Attribution 4.0 License](https://creativecommons.org/licenses/by/4.0/). Further distribution of this work must maintain attribution to the author(s) and the published article's title, journal citation, and DOI.

## 1. Introduction

Metasurfaces have become an extremely active area in photonics research as they enable optical properties that are often impossible to achieve using bulk materials [1,2]. Metasurfaces are typically made using a collection of metallic or dielectric “meta-atoms”, which alter the properties of the metasurface due to, for example, excitation of resonances. In the case of dielectric metasurfaces, resonant Mie modes can be excited within the individual meta-atoms. Several extraordinary effects have been demonstrated using this approach, ranging from unidirectional scattering to high harmonic generation [3–6].

One particularly useful application of dielectric metamaterials is enhancement of optical absorption [7–14]. In fact, perfect absorption can be achieved in subwavelength-thickness metasurfaces by exciting two carefully tuned Mie modes [15,16]. This functionality has opened doors to more efficient architectures for optoelectronic devices, where the metasurface can eliminate reflection loss and enable complete absorption of incident photons in a relatively thin layer. Perfectly absorbing metasurface designs have already been used to enhance efficiency of

terahertz (THz) detectors [11] along with many other applications across the electromagnetic spectrum [17–24].

Despite the far-reaching potential of perfect absorption and recent investigations of the physical mechanisms [15,16,25,26], its application in optoelectronic devices has been somewhat limited. This can be attributed to the fact that designing perfectly absorbing metasurfaces for a desired wavelength or material is highly non-trivial [8]. In practice, a stringent set of conditions need to be satisfied simultaneously: the resonant modes must be of opposite symmetries (one odd mode and one even with respect to the metasurface plane), both must be centered at the desired wavelength (mode degeneracy), and each mode must be critically coupled to the incident field (i.e. the radiative losses of the mode must match the mode's absorption loss at this wavelength). Realizing these conditions is particularly challenging when working near the interband transition edge of direct bandgap semiconductors, where intrinsic material absorption decreases rapidly with photon energy. In this highly dispersive region, the change in intrinsic material absorption inevitably leads to a breakdown of the critical coupling condition when scaling the geometry of the metasurface.

Consequently, the process of designing perfectly absorbing metasurfaces often involves trial and error, which can be time-consuming and unreliable at finding the optimum solution. Genetic optimization [9] and deep learning [27] algorithms have recently been explored as alternative approaches to this design problem, however these methods don't necessarily reveal the underlying physics and require pre-calculated training sets of data.

Here we provide a systematic and intuitive process for designing perfectly absorbing metasurfaces for a desired wavelength of operation, even when the intrinsic material absorption varies dramatically with wavelength. Our design is based on exciting two degenerate magnetic dipole modes of opposite symmetries. To facilitate an intuitive understanding of the design and the underlying physics, we describe the effects of all geometrical parameters of the metasurface on the modes using numerical modeling and confirm the key effects experimentally. We then devise a three-step process allowing us to engineer the metasurface for perfect absorption at a desired wavelength of operation. As a practical demonstration, we show the effect of greatly enhanced absorption for two exemplary metasurfaces made of low-temperature (LT) grown GaAs. One of these is designed for the high intrinsic absorption region, at 790 nm, sufficiently high above the GaAs bandgap; and the second at 875 nm, near the bandgap edge. At this wavelength, the intrinsic absorption of LT GaAs approaches zero [28] and is poorly defined due to Arsenic inclusions and crystal defects [29,30]. Such high absorption has not been previously demonstrated in a sub-wavelength thickness GaAs structure at this wavelength.

This method for creating a perfectly absorbing metasurface can be used for improving efficiency of optoelectronic devices. The particular designs discussed here can be used for fast LT GaAs photoconductive switches for THz detectors, emitters and modulators. These devices are commonly operated with ultrafast lasers in a wavelength range from 700 to 850 nm and are built from low-temperature grown or ion-implanted materials [31]. However, the method is also readily applicable to a wide range of semiconductor materials, and could improve performance of devices such as sensors and solar cells across the electromagnetic spectrum.

## 2. Effects of geometrical parameters

The perfect absorption effect considered here relies on exciting two degenerate and critically-coupled modes with opposite symmetry [15]. In theory, any two modes that satisfy these conditions can be used for perfect absorption. Following the recent demonstration of perfect absorption at 800 nm (in the highly absorbing region of GaAs) [11], we select two magnetic dipole modes, one with the magnetic field vector oriented in the metasurface plane, and the other one perpendicular to it. We refer to these modes as  $M_x$  (in-plane) and  $M_z$  (out-of-plane) dipoles hereafter (Fig. 1(a)).

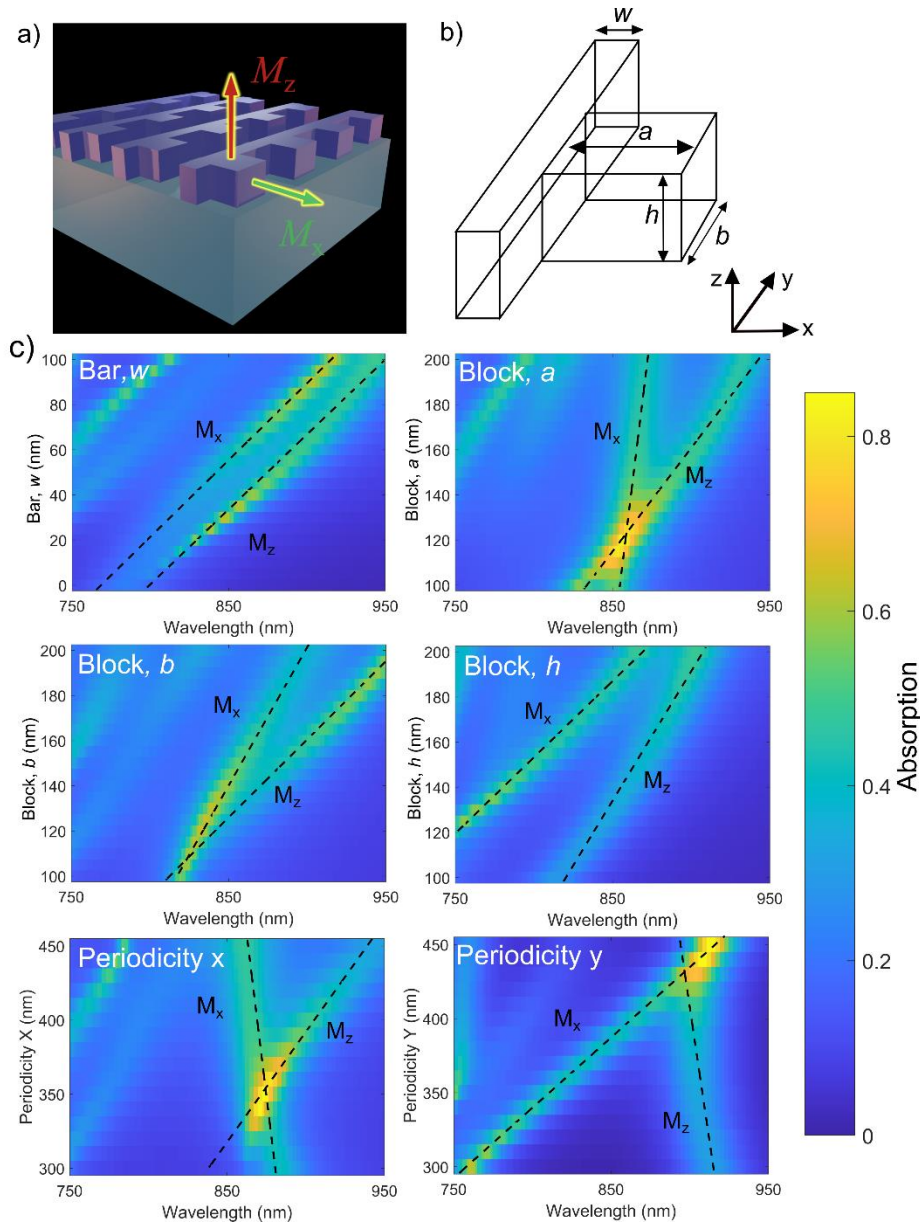


**Fig. 1.** a) Illustration of the perfectly absorbing metasurface, showing magnetic dipoles in  $x$ -direction (green) and  $z$ -direction (red) in one unit cell. b) Schematic diagram of unit cell. c) Simulated absorption for varying geometrical parameters. All other parameters remain constant ( $w = 60$  nm,  $a = 160$  nm,  $b = 160$  nm,  $h = 200$  nm, periods = 400 nm). Real and imaginary permittivities are modelled as constants ( $n = 3.684$   $\kappa = 0.01$ ). Lines show the approximate tuning of each mode with the varying parameter.

Both  $M_x$  and  $M_z$  dipoles exist in a dielectric cube. The former can be excited by a linearly polarized plane wave with the electric field vector oriented along the  $y$ -axis (Fig. 1(b)); whereas the latter is a dark mode for normal incidence excitation. However, by breaking the cube symmetry and introducing a bar on one side of the cube, both the  $M_x$  mode and the  $M_z$  mode can be excited by the plane wave at normal incidence [32]. We will show later that the bar also can serve as key element for adjusting the wavelength of operation. Furthermore, the bar provides a conducting channel between resonators, which could be used in optoelectronic devices [7,11]. The metasurface is constructed by repeating a unit cell consisting of the cube and bar in a square lattice with lattice constant  $L$  as illustrated in Fig. 1(a).

To achieve perfect absorption at a desired wavelength, the modes must be degenerate, and centered at the chosen wavelength. Figure 1(c) illustrates how the resonant wavelengths for the  $M_x$  and  $M_z$  modes depend on each geometrical parameter. Several points of enhanced absorption can be seen where the two modes cross each other. Simply by selecting the parameters at one of these points gives the required mode degeneracy (for practical applications, we show how to achieve the condition of mode degeneracy experimentally in the supplementary information). The obvious way to tune the modes to a desired wavelength is by scaling the metasurface in all dimensions. However, this is not always practical because the thickness of the metasurface is set during the wafer growth process. Scaling metasurface dimensions only in the  $xy$ -plane will, on the other hand, leads to a loss of mode degeneracy.

To develop an alternative approach for achieving perfect absorption for a wide range of wavelengths and intrinsic absorption of the constituent semiconductor material, we consider tuning of the magnetic dipole mode wavelengths and radiative losses with individual geometrical parameters of the metasurface. It can be seen in Fig. 1(c) that the two modes tune as functions of most metasurface parameters at different rates, resulting in a breakdown of mode degeneracy and the perfect absorption condition. However, the bar width affects both modes at similar rates over a wide range of wavelengths. Using this unique bar width dependence, we can tune the two modes without losing mode degeneracy.

Figure 1(c) also shows that varying the periodicity in either  $x$  or  $y$ -direction affects primarily only one mode,  $M_z$  or  $M_x$  respectively, while the wavelength of the other mode remains relatively unchanged. Adjusting the two periodicities simultaneously therefore provides another method to maintain mode degeneracy. At the same time, the metasurface periodicity affects the radiative losses of the modes, and consequently their critical coupling conditions [8]. Therefore, we may use the periodicity for achieving the critical coupling condition without losing the mode degeneracy.

Using these trends, we develop a three-step process, which adjusts the metasurface geometry for achieving perfect absorption at a desired wavelength. Starting with a design where modes are degenerate, we first adjust the bar width in order to tune the mode resonant wavelength. In the second step, we tune the radiative losses by adjusting the both periodicities of the square lattice, and approach the critical coupling condition with only a small effect on the mode wavelength. Step 2 results in close-to-perfect absorption. For the best performance, an additional numerical optimization of the central block parameters can be done to regain full overlap of the modes and reach the perfect absorption condition. In the following sections, the physical mechanism behind this process is discussed in detail.

### 2.1. Bar width

In order to investigate the shift of the two modes with the width of the bar,  $w$ , we first design a structure with the modes  $M_x$  and  $M_z$  positioned at 790 nm, similarly to the structure in Ref. [11]. We then numerically simulate absorption for metasurfaces with the bar width varied from 0 nm (corresponding to the case of symmetric rectangular dielectric resonator) to 160 nm. Figure 2(b) shows the simulated absorption spectra for different bar widths as a color map. For illustration

purposes, we first consider a non-dispersive material (i.e. fixed material parameters:  $n = 3.684$  and  $\kappa = 0.087$ , are constants independent of the wavelength, typical of GaAs at 800 nm). We also simulate the metasurface surrounded above and below by a uniform dielectric material, with the refractive index of  $n = 1.57$  - typical for transparent substrates (e.g. glass). A highly absorbing band can be seen spanning from 700 to 950 nm where both modes shift together with bar width. At a bar width of 40 nm maximum absorption of 99.88% is achieved. For the purpose of this paper we define perfect absorption as  $> 98\%$  due to the simulation accuracy which is limited by the finite simulation mesh (see the supplemental document for more information). Individual higher order modes can be seen to the left, at shorter wavelengths. However, those modes do not cross each other and do not show perfect absorption, despite high material absorption in GaAs in this region.

Figure 2(d),(e) illustrates the mode profiles of the  $M_x$  and  $M_z$  modes for two different bar widths: 40 nm and 100 nm. The circled peaks in the spectra correspond to the peaks shown by arrows in Fig. 2(b), where the  $M_x$  and  $M_z$  mode both sit at the same wavelength. The mode profiles at peak absorption wavelength show the change in modes with increasing bar width, and provide insight into the physical mechanism behind the shifting of the modal wavelengths with bar width. When bar width increases, the area of the central block structure in the  $xy$ -plane is expanded. This increases the mode volume and therefore the wavelength of the  $M_z$  mode resonance, as the circulating E-field corresponding to the  $M_z$  mode sits in the  $xy$ -plane. Increasing the bar width also shifts the  $M_x$  mode from the block toward the bar where mode volume also increases. As a result, the wavelength of the  $M_x$  mode increases. Both modes therefore shift to longer wavelengths.

The simulations show that the rate of this shift for both modes is similar, and therefore by tuning the bar width we can adjust the frequency of the modes by roughly the same amount. The same mode behavior occurs if we consider the index dispersion in GaAs [28]: the modes still shift together and over a range of wavelengths across the bandgap, remaining approximately degenerate (Fig. 2(c)). This allows us to choose the operation frequency of the metasurface simply by adjusting one single parameter - the bar width.

The simulations with dispersive material parameters near the band-gap also highlights the fact that the mode degeneracy is only a necessary and not sufficient condition. We observe a large variation in the peak absorption as the bar width changes. At longer wavelengths intrinsic absorption decreases and no longer matches the radiative loss of the mode. As a result, the modes move away from the critical coupling condition and the effect of total absorption disappears.

## 2.2. Periodicity

In order to satisfy the critical coupling condition, we now tune the periodicity of the structure by changing the size of the unit cell in both the  $x$ - and  $y$ -directions without adjusting the resonator and bar sizes. It has been demonstrated in several other metasurface systems that periodicity alters the collective behavior of the resonators including the radiative losses [8,33–35]. At the same time, the effect on the Mie resonance wavelength in our metasurface is relatively small. Specifically, the change in periodicity by 20% results in the mode wavelength shift of only 6-7%. Figure 3 shows the tuning of periodicity from 340 nm to 440 nm for a 40 nm bar structure, using the Palik model for GaAs. The maximum absorption of 99.9% is achieved at a periodicity of 395 nm.

To illustrate the impact of material absorption, Fig. 3(c) shows how absorption of the two degenerate modes changes for varying intrinsic material absorption. For a set periodicity and metasurface parameters, it can be seen that the peak absorption first rises sharply as the extinction coefficient,  $\kappa$  is varied from 0.001 to 0.05. At a particular  $\kappa$  value of 0.08 the metasurface reaches perfect absorption. This value of material absorption corresponds to the critical coupling condition, i.e. the absorption of the modes matches the radiative loss of the modes. If the material

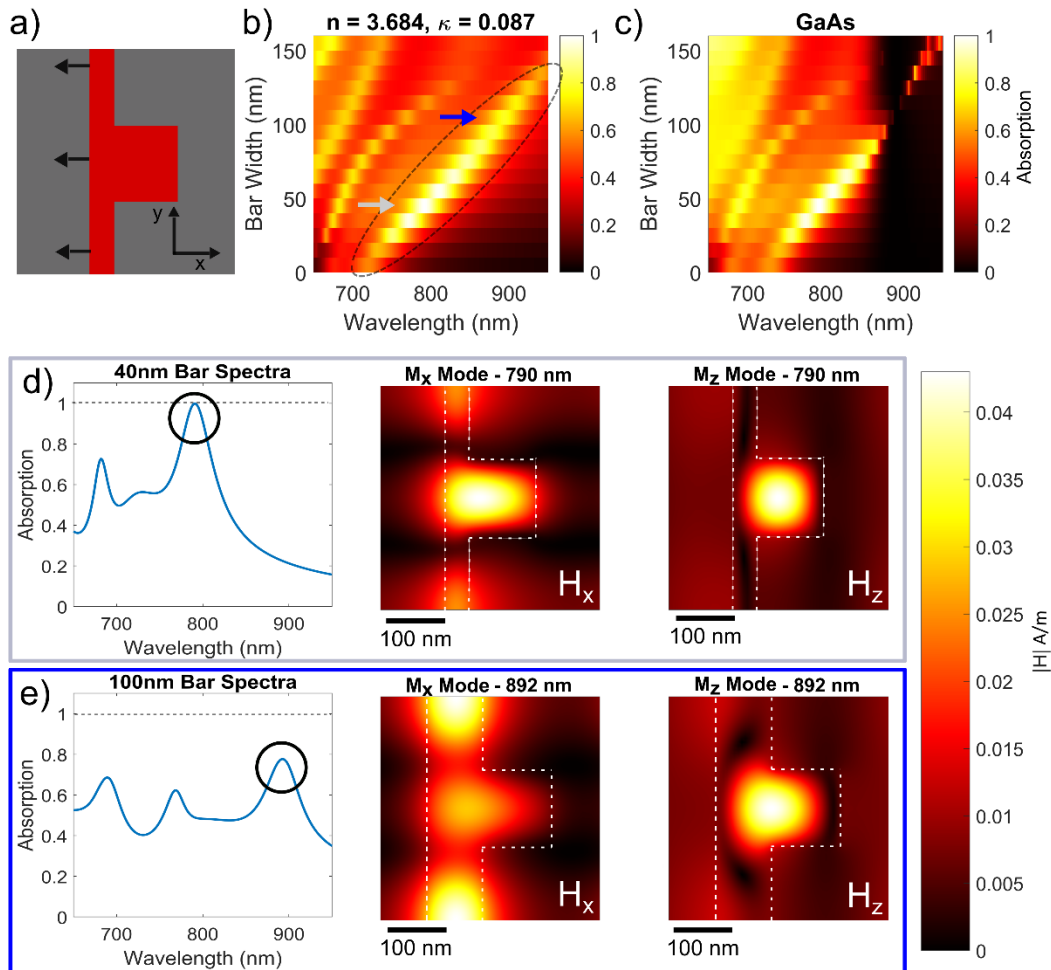


**Fig. 2.** Effect of the bar width: a) Schematic diagram of the unit cell illustrating the increase in bar width. b) & c) Simulated total absorption for varying bar width. In b) real and imaginary permittivities are modelled as constants ( $n = 3.684$ ,  $\kappa = 0.087$ ), whereas in c) real and imaginary permittivities vary according to the GaAs Palik model. d) Simulated absorption and magnetic field profiles at the peak absorption wavelength (790 nm) for the 40 nm bar width (grey arrow in b, for constant permittivities). e) Simulated absorption with magnetic field profiles at the peak absorption wavelength (892 nm) for the 80 nm bar width (blue arrow in b, constant permittivities). The magnetic field maps represent cross-section in the  $xy$ -plane. All parameters remain constant ( $a = 125$  nm,  $b = 140$  nm,  $h = 200$  nm, periods = 395 nm).

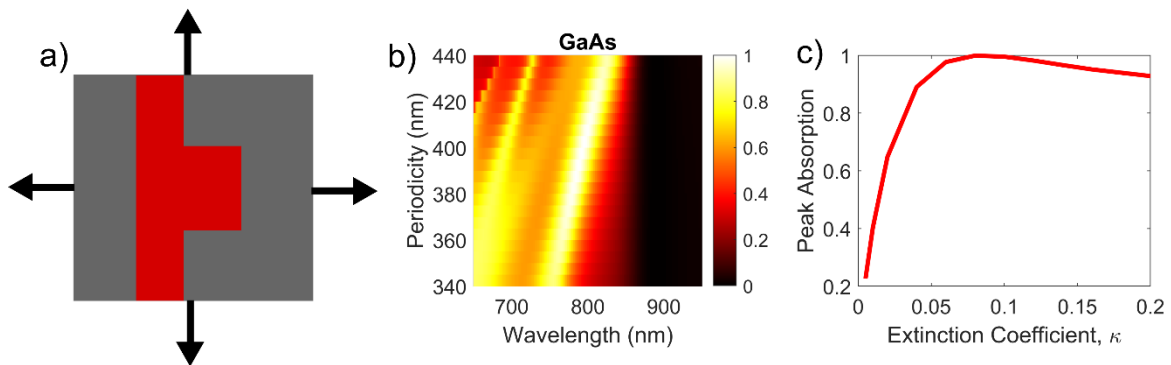


**Fig. 3.** Effect of periodicity tuning: a) Diagram demonstrating periodicity increase in both x- and y-directions. The bar and block size remain constant ( $w = 40\text{nm}$ ,  $a = 125\text{ nm}$ ,  $b = 140\text{nm}$ ,  $h = 200\text{ nm}$ ). b) Simulated total absorption for varying periodicity. Real and imaginary permittivities vary according to the GaAs Palik model. c) Simulated maximum absorption for varying extinction coefficient,  $\kappa$ . Periodicity and structure parameters are fixed.

absorption is increased beyond this value, the structure moves away from the critically coupled condition and overall absorption of the metasurface decreases. A similar process happens when the periodicity is modified in Fig. 3(b), except here the radiative losses are varied rather than the material absorption.

### 2.3. Central block size

Whilst the bar width enables tuning of the  $M_x$  and  $M_z$  dipole together and the periodicity allows us to adjust radiative loss, the modes may drift apart during these steps for large parameter changes. The impact of mode splitting on peak absorption varies with wavelength. In the region where intrinsic absorption is high, the mode splitting does not largely affect peak absorption: we find that  $>90\%$  absorption can be achieved after adjusting the periodicity without further changes. For wavelengths where the intrinsic loss is low, the splitting plays a more significant role. For example, in Fig. 2(c), the modes visibly split into two separate absorption peaks in the region of 950 nm. The difference is due to the linewidths of the modes.

If a mode splitting occurs, the modes can be re-matched and absorption maximized by a process of local ‘particle swarm’ numerical optimization of the central block parameters,  $a$  and  $b$ . We note that the block thickness,  $h$ , also affects the mode frequencies, however this parameter is fixed at the wafer growth stage and it is less practical to adjust during the fabrication process.

## 3. Experimental results

We now experimentally verify the effects of the bar width and periodicity. Metasurfaces with different bar widths and periodicities were fabricated from a 200 nm epilayer of LT-GaAs using electron-beam lithography and etching. Figures 4(a),(c) show scanning electron microscope images of the metasurface pattern etched into the epilayer. The 200 nm thick metasurfaces are then transferred onto sapphire substrates. As a result, the metasurfaces are submerged in epoxy ( $n = 1.57$ ), which bonds the metasurface to the substrate, while the half-space above the metasurface is air. Fabrication details are described in the supplemental document.

Firstly, we discuss the effect of the bar width. Figure 4 shows measured transmission spectra for a set of metasurfaces with varied bar widths, along with simulated spectra for structures with similar dimensions to the fabricated devices. For each structure, there is a deep dip in

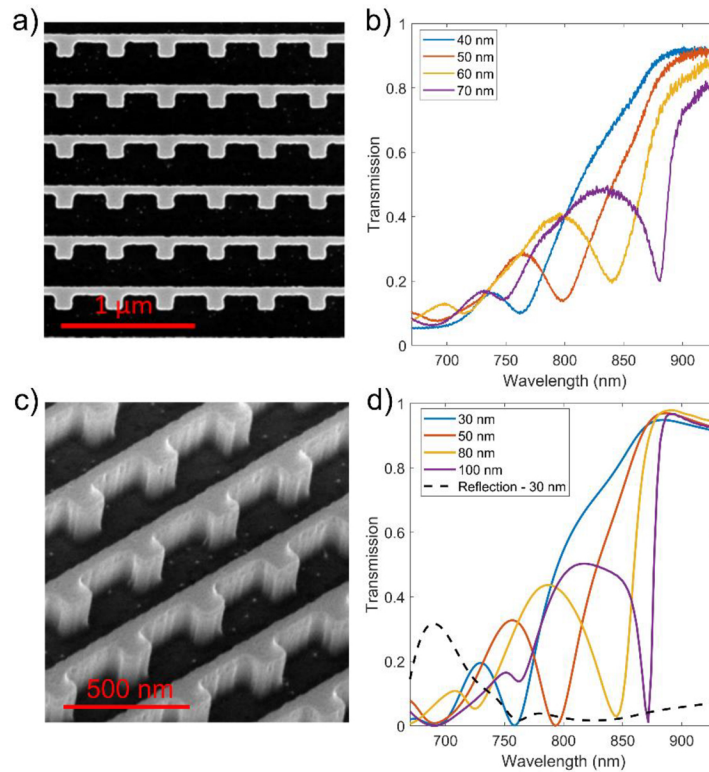


**Fig. 4.** Effect of the bar width in experiments and simulations: a) Scanning Electron Microscope (SEM) image of metasurface (top view). b) Transmission spectra measured in fabricated structures with block dimensions  $a \sim 120$  nm  $b \sim 140$  nm for varying bar width. c) Scanning Electron Microscope (SEM) image of metasurface, measured at oblique incidence. d) Transmission spectra simulated for several bar widths, including reflection spectra for structure with 30 nm bar width. Other device parameters chosen to match fabricated structures in b.

transmission. Although it appears as a single mode feature, two modes overlap at this wavelength. This feature represents strongly enhanced absorption. As the bar width is varied the transmission dip shifts in wavelength without splitting into two peaks, demonstrating the ability to tune the two mode wavelengths simultaneously with the bar width.

We note that due to the proximity effect in electron beam lithography [36], the increase in the nominal bar width from 40 nm to 70 nm results in superlinear increase of the fabricated bar width, as well as in small increase of the central block size. These changes are too small ( $< 10$  nm) to be evaluated precisely from SEM images. Nevertheless, they result in apparent higher rate of wavelength tuning in the fabricated structures in comparison to simulations. Therefore, we simulate a wider range of bar widths and provide their transmission spectra in Fig. 4(d). We find good agreement between these simulations and the experiment.

We also note that in the simulations, the metasurface is almost fully transparent at 890 nm. This is the result of a standard GaAs model, which lacks accuracy to describe LT GaAs permittivity in the long wavelength region. The experimental results on the other hand show lower transmission in the long wavelength region, indicating that there is non-negligible absorption, likely due to As islands and crystal defects in LT GaAs [29,30].

For smaller bar thicknesses, the minimum transmission is  $\sim 0.1$ , suggesting that the structure is close to the critical coupling condition, and therefore near perfect absorption. The simulated measurements confirm this, as for the 30nm bar width, both reflection and transmission are near-zero, meaning absorption is  $> 0.95$ . However, once the mode wavelengths are increased using the bar width, the structure loses the condition of critical coupling and the peak absorption decreases (see supplemental document). High absorption is now regained by varying the periodicity. Figure 5 shows measured (a) and simulated (b) transmission spectra for several metasurfaces with varied periodicities whilst other parameters are fixed. In Fig. 5(a), the minimum in transmission decreases with increasing periodicity. This is a consequence of the changing radiative loss of the metasurface with periodicity – as the period increases the structure moves closer to the critical coupling condition where the radiative loss matches the absorption loss for each mode.

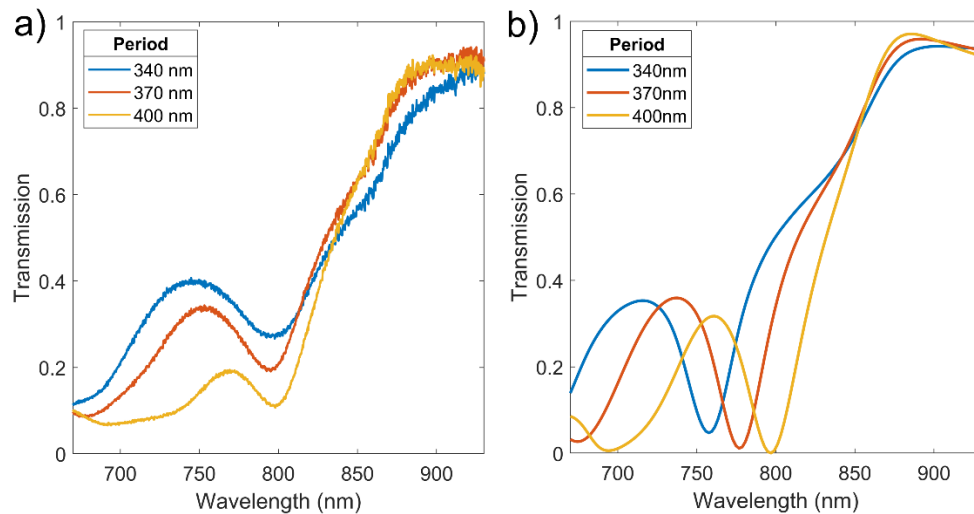


**Fig. 5.** Effect of periodicity in experiment and simulations: a) Transmission spectra measured in fabricated structures for varying periodicity. b) Transmission spectra simulated for several periodicities. Other device parameters chosen to match fabricated structures in a.

We note that in the fabricated structures there is very little change in peak absorption wavelength with periodicity, however for the simulated structures a notable change is observed. We believe this is a consequence of the proximity effect in the electron beam lithography stage of fabrication. For smaller periodicities (340 nm), neighboring resonators are much closer to each other and the proximity effect results in an increased size of the central block and bar. Consequently, the resonant wavelength increases in comparison to the simulated structures, where the geometry remains constant for all periodicities.

The ability to tune the radiative losses with periodicity in the fabrication process is particularly advantageous when fabricating structures close to the bandgap edge. As previously mentioned, in this spectral region published models for GaAs imaginary permittivity may not closely match LT-GaAs due to the presence of defects, making it difficult to use simulations for refining optimum metasurface geometry. However, varying the periodicity in the fabrication process allows us to optimize the radiative loss and match it to the real absorption losses. This can lead to a slightly different optimum periodicity in the simulation compared to the fabricated structures.

#### 4. Enhancing absorption near GaAs bandgap

We now use the perfectly absorbing structure designed in Section 2 for 790 nm, and apply the three-step design method to enhance absorption near the bandgap wavelength, where the intrinsic absorption of GaAs is significantly lower (less than half that at 790 nm). First, we increase the bar width to 80 nm to position the peak absorption close to the bandgap wavelength (860 nm); then by sweeping the periodicity numerically, we find a period for which the absorption level is maximum. For the 80 nm bar, the required period is 380 nm, and it yields a peak absorption of 88%. Finally, by optimizing the block size, the peak absorption can be increased to 98% if the block size is increased by 15 nm in the x-direction and 25 nm in the y-direction (during the optimization process the size of the block is varied in increments of 5 nm).

In Fig. 6(a),(b) we show simulated optical absorption, transmission and reflection spectra after the optimization process, and compare it to the metasurface design for 790 nm. The new design now shows the absorption peak at 860 nm. In both cases, the peak absorption reaches as high as 98%, despite the significant difference in intrinsic material absorption at 790 nm and 860 nm. The reduced intrinsic absorption at 860 nm affects the linewidth of the absorption peak, which is significantly narrower in comparison to the 790 nm peak.

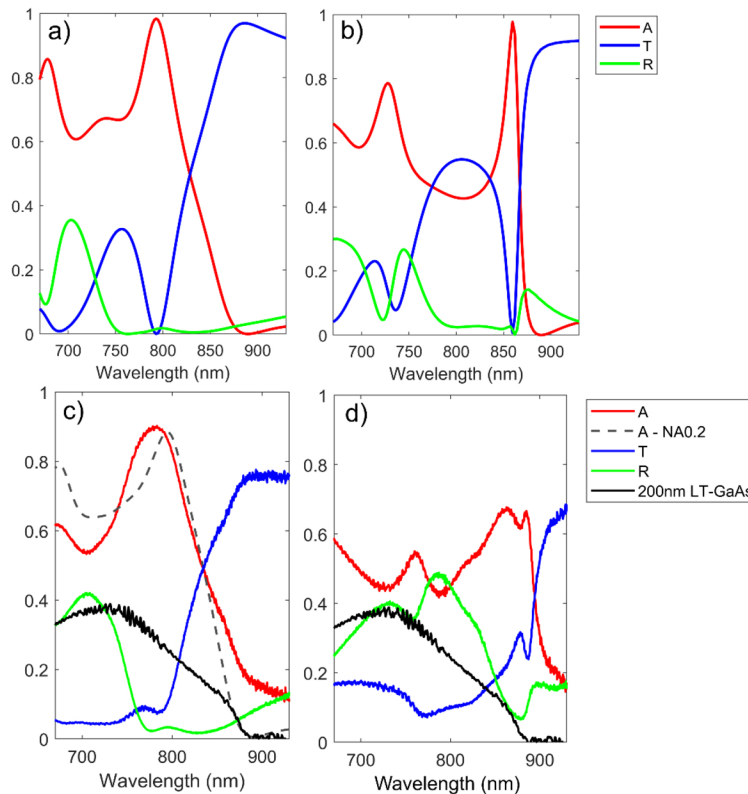


**Fig. 6.** Enhanced absorption in metasurfaces in the regions of high and low intrinsic absorption. Simulated optical properties of perfectly absorbing structure at (a) 790 nm and (b) 860 nm. Measured optical properties of fabricated metasurfaces showing enhanced absorption at 790 nm (c) and 875 nm (d). Absorption for a 200 nm unstructured layer of LT-GaAs is shown for comparison (black lines), as well as absorption for the 790 nm metasurface when illuminated by a Gaussian beam with numerical aperture of 0.2 (c – gray dashed line).

In Fig. 6(c),(d) the experimentally measured absorption spectra are shown for two fabricated structures with similar dimensions as in Fig. 6(a),(b). As with the simulated designs, the first fabricated structure shows a broad absorption peak centered around 790 nm, whereas the second structure shows enhanced absorption at 875 nm. For comparison, we also show an experimentally measured absorption spectrum for an unpatterned (uniform) 200 nm thick LT GaAs layer (black line), where absorption gradually decreases with increasing wavelength, approaching zero around 875 nm. In contrast, the metasurface of the same thickness absorbs up to  $\sim 70\%$  of incident light at that wavelength, indicating a strong absorption enhancement effect. For both structures, we see a significant dip in both transmission and reflection at the peak absorption wavelength.

The peak absorption levels in both fabricated metasurfaces are not as high as predicted in the simulations. This is due to the fact that the experimental spectra were measured using a focused optical beam with  $NA \sim 0.16$ , rather than the plane wave used in simulations. For such a beam, the peak broadens, and absorption decreases by  $\sim 10\%$  according to our numerical simulations (gray dashed line in Fig. 6(c)). In addition, for the structure in Fig. 6(d) the two modes are not perfectly aligned, as is evident from the two separate peaks in the spectrum. In this region of the spectrum the lack of strong material absorption causes the modes to become much narrower and therefore more sensitive to mode misalignment. In principle, similarly to the step described in Section 2.3, small adjustments of the central block size can be performed in order to align the two modes.

Despite these small discrepancies, the experimentally observed spectrum clearly shows a resonant absorption enhancement of 3-fold for the 790 nm structure and over 15-fold for the 875 nm structure in comparison to the unpatterned LT-GaAs layer.

## 5. Conclusion

In conclusion, we demonstrate that using the scheme of perfect absorption based on two degenerate magnetic dipole modes, we can experimentally achieve strong enhancement of optical absorption in LT GaAs based metasurfaces within a wide range of intrinsic material absorption. We identified two geometrical parameters of the structure which enable concurrent tuning of two magnetic dipole modes with similar rates and maximizing of absorption through adjustment of radiative losses. Tuning these parameters allows us to adapt the perfectly absorbing metasurface design for operation across a range of wavelengths with significant variations of intrinsic material absorption, using a straightforward prescriptive technique. Our method takes the guesswork out of designing metasurfaces for a desired wavelength of operation, or adjusting the metasurface design to achieve the condition of perfect absorption. We anticipate that this method will lead to wider use of all-dielectric perfectly-absorbing metasurfaces for a variety of applications. Specifically, such metasurfaces can be used as efficient photoconductive elements in optoelectronic devices and with the adaptable design, they can be tailored to desired laser wavelengths and for other materials.

## Funding

Engineering and Physical Sciences Research Council (EP/L015277/1, EP/L015455/1, EP/P021859/1); U.S. Department of Energy.

## Acknowledgments

This work was supported by the U.S. Department of Energy, Office of Basic Energy Sciences, Division of Materials Sciences and Engineering and performed, in part, at the Center for Integrated Nanotechnologies, an Office of Science User Facility operated for the U.S. Department of Energy, Office of Science. Sandia National Laboratories is a multimission laboratory managed and operated by National Technology and Engineering Solutions of Sandia, LLC, a wholly owned subsidiary of Honeywell International, Inc., for the U.S. Department of Energy's National Nuclear

Security Administration under Contract No. DE-NA0003525. OM, LH and TS acknowledge the support of the EPSRC (EP/P021859/1, EP/L015455/1, EP/L015277/1).

This paper describes objective technical results and analysis. Any subjective views or opinions that might be expressed in the paper do not necessarily represent the views of the U.S. Department of Energy or the United States Government.

## Disclosures

The authors declare no conflicts of interest.

See [Supplement 1](#) for supporting content.

## References

1. I. Brener, S. Liu, I. Staude, J. Valentine, and C. L. Holloway, *Dielectric Metamaterials: Fundamentals, Designs and Applications*, 1st ed. (Woodhead Publishing, 2019).
2. H. T. Chen, A. J. Taylor, and N. Yu, "A review of metasurfaces: Physics and applications," *Rep. Prog. Phys.* **79**(7), 076401 (2016).
3. I. Staude, T. Pertsch, and Y. S. Kivshar, "All-Dielectric Resonant Meta-Optics Lightens up," *ACS Photonics* **6**(4), 802–814 (2019).
4. A. I. Kuznetsov, A. E. Miroshnichenko, M. L. Brongersma, Y. S. Kivshar, and B. Luk'yanchuk, "Optically resonant dielectric nanostructures," *Science* **354**(6314), aag2472 (2016).
5. S. Kruk and Y. Kivshar, "Functional Meta-Optics and Nanophotonics Govern by Mie Resonances," *ACS Photonics* **4**(11), 2638–2649 (2017).
6. S. Jahani and Z. Jacob, "All-dielectric metamaterials," *Nat. Nanotechnol.* **11**(1), 23–36 (2016).
7. O. Mitrofanov, T. Siday, R. J. Thompson, T. S. Luk, I. Brener, and J. L. Reno, "Efficient photoconductive terahertz detector with all-dielectric optical metasurface," *APL Photonics* **3**(5), 051703 (2018).
8. X. Ming, X. Liu, L. Sun, and W. J. Padilla, "Degenerate critical coupling in all-dielectric metasurface absorbers," *Opt. Express* **25**(20), 24658 (2017).
9. X. Liu, K. Fan, I. V. Shadrivov, and W. J. Padilla, "Experimental realization of a terahertz all-dielectric metasurface absorber," *Opt. Express* **25**(1), 191 (2017).
10. V. E. Babicheva and A. B. Evlyukhin, "Resonant Lattice Kerker Effect in Metasurfaces With Electric and Magnetic Optical Responses," *Laser Photonics Rev.* **11**(6), 1700132 (2017).
11. T. Siday, P. P. Vabishchevich, L. Hale, C. T. Harris, T. S. Luk, J. L. Reno, I. Brener, and O. Mitrofanov, "Terahertz Detection with Perfectly-Absorbing Photoconductive Metasurface," *Nano Lett.* **19**(5), 2888–2896 (2019).
12. J. Y. Suen, K. Fan, and W. J. Padilla, "A Zero-Rank, Maximum Nullity Perfect Electromagnetic Wave Absorber," *Adv. Opt. Mater.* **7**(8), 1801632 (2019).
13. X. Zhao, Y. Wang, J. Schalch, G. Duan, K. Cremin, J. Zhang, C. Chen, R. D. Averitt, and X. Zhang, "Optically Modulated Ultra-Broadband All-Silicon Metamaterial Terahertz Absorbers," *ACS Photonics* **6**(4), 830–837 (2019).
14. H. A. Atwater and A. Polman, "Plasmonics for improved photovoltaic devices," *Nat. Mater.* **9**(3), 205–213 (2010).
15. J. R. Piper, V. Liu, and S. Fan, "Total absorption by degenerate critical coupling," *Appl. Phys. Lett.* **104**(25), 251110 (2014).
16. R. Alaee, M. Albooyeh, and C. Rockstuhl, "Theory of metasurface based perfect absorbers," *J. Phys. D: Appl. Phys.* **50**(50), 503002 (2017).
17. A. K. Azad, W. J. M. Kort-Kamp, M. Sykora, N. R. Weisse-Bernstein, T. S. Luk, A. J. Taylor, D. A. R. Dalvit, and H. T. Chen, "Metasurface Broadband Solar Absorber," *Sci. Rep.* **6**(1), 6–11 (2016).
18. C. C. Chang, W. J. M. Kort-Kamp, J. Nogan, T. S. Luk, A. K. Azad, A. J. Taylor, D. A. R. Dalvit, M. Sykora, and H. T. Chen, "High-Temperature Refractory Metasurfaces for Solar Thermophotovoltaic Energy Harvesting," *Nano Lett.* **18**(12), 7665–7673 (2018).
19. N. Liu, M. Mesch, T. Weiss, M. Hentschel, and H. Giessen, "Infrared perfect absorber and its application as plasmonic sensor," *Nano Lett.* **10**(7), 2342–2348 (2010).
20. S. Kim, M. S. Jang, V. W. Brar, K. W. Mauser, L. Kim, and H. A. Atwater, "Electronically Tunable Perfect Absorption in Graphene," *Nano Lett.* **18**(2), 971–979 (2018).
21. M. D. Goldflam, E. A. Kadlec, B. V. Olson, J. F. Klem, S. D. Hawkins, S. Parameswaran, W. T. Coon, G. A. Keeler, T. R. Fortune, A. Tauke-Pedretti, J. R. Wendt, E. A. Shaner, P. S. Davids, J. K. Kim, and D. W. Peters, "Enhanced infrared detectors using resonant structures combined with thin type-II superlattice absorbers," *Appl. Phys. Lett.* **109**(25), 251103 (2016).
22. S. Liu, P. P. Vabishchevich, A. Vaskin, J. L. Reno, G. A. Keeler, M. B. Sinclair, I. Staude, and I. Brener, "An all-dielectric metasurface as a broadband optical frequency mixer," *Nat. Commun.* **9**(1), 2507 (2018).

23. J. Y. Jung, K. Song, J. H. Choi, J. Lee, D. G. Choi, J. H. Jeong, and D. P. Neikirk, "Infrared broadband metasurface absorber for reducing the thermal mass of a microbolometer," *Sci. Rep.* **7**(1), 1–8 (2017).
24. K. Fan, J. Y. Suen, X. Liu, and W. J. Padilla, "All-dielectric metasurface absorbers for uncooled terahertz imaging," *Optica* **4**(6), 601 (2017).
25. Y. Ra'di, C. R. Simovski, and S. A. Tretyakov, "Thin Perfect Absorbers for Electromagnetic Waves: Theory, Design, and Realizations," *Phys. Rev. Appl.* **3**(3), 037001 (2015).
26. C. M. Watts, X. Liu, and W. J. Padilla, "Metamaterial electromagnetic wave absorbers," *Adv. Mater.* **24**(23), OP98–OP120 (2012).
27. C. C. Nadell, B. Huang, J. M. Malof, and W. J. Padilla, "Deep learning for accelerated all-dielectric metasurface design," *Opt. Express* **27**(20), 27523 (2019).
28. E. D. Palik, *Handbook of Optical Constants of Solids* (Academic, 1998) Vol.2 Chap.14.
29. H. C. Casey, D. D. Sell, and K. W. Wecht, "Concentration dependence of the absorption coefficient for n- and p-type GaAs between 1.3 and 1.6 eV," *J. Appl. Phys.* **46**(1), 250–257 (1975).
30. I. Ohbu, M. Takahama, and K. Hiruma, "Defects in low-temperature-grown GaAs annealed at 800°C," *Appl. Phys. Lett.* **61**(14), 1679–1681 (1992).
31. N. M. Burford and M. O. El-Shenawee, "Review of terahertz photoconductive antenna technology," *Opt. Eng.* **56**(1), 010901 (2017).
32. S. Campione, S. Liu, L. I. Basilio, L. K. Warne, W. L. Langston, T. S. Luk, J. R. Wendt, J. L. Reno, G. A. Keeler, I. Brener, and M. B. Sinclair, "Broken Symmetry Dielectric Resonators for High Quality Factor Fano Metasurfaces," *ACS Photonics* **3**(12), 2362–2367 (2016).
33. M. Wenclawiak, K. Unterrainer, and J. Darmo, "Cooperative effects in an ensemble of planar meta-atoms," *Appl. Phys. Lett.* **110**(26), 261101 (2017).
34. J. Keller, J. Haase, F. Appugliese, S. Rajabali, Z. Wang, G. L. Paravicini-Bagliani, C. Maissen, G. Scalari, and J. Faist, "Superradiantly Limited Linewidth in Complementary THz Metamaterials on Si-Membranes," *Adv. Opt. Mater.* **6**(16), 1800210 (2018).
35. I. Sersic, M. Frimmer, E. Verhagen, and A. F. Koenderink, "Electric and Magnetic Dipole Coupling in Near-Infrared Split-Ring Metamaterial Arrays," *Phys. Rev. Lett.* **103**(21), 213902 (2009).
36. T. H. P. Chang, "Proximity effect in electron-beam lithography," *J. Vac. Sci. Technol. (N. Y., NY, U. S.)* **12**(6), 1271–1275 (1975).